

Local dynamic responses of magnetic reconnection to three-dimensional perturbations in a laboratory plasma

Cite as: Phys. Plasmas **31**, 022108 (2024); doi: 10.1063/5.0187992

Submitted: 17 November 2023 · Accepted: 28 January 2024 ·

Published Online: 20 February 2024



View Online



Export Citation



CrossMark

Jinlin Xie,^{1,2,a)} Peiyun Shi,^{1,b)} Hantao Ji,^{1,3} Jonathan Jara-Almonte,¹ Jongsoo Yoo,¹ Yukehi Okunishi,¹ Seth Dorfman,^{4,5} and Masaaki Yamada¹

AFFILIATIONS

¹Princeton Plasma Physics Laboratory, Princeton, New Jersey 08543, USA

²Department of Plasma Physics and Fusion Engineering, University of Science and Technology of China, Hefei 230026, China

³Department of Astrophysical Sciences, Princeton University, Princeton, New Jersey 08544, USA

⁴Space Science Institute, Boulder, Colorado 80301, USA

⁵Department of Physics and Astronomy, University of California, Los Angeles, California 90095, USA

^{a)}Electronic mail: jlxie@ustc.edu.cn

^{b)}Author to whom correspondence should be addressed: pshi@pppl.gov

ABSTRACT

The dynamic responses of magnetic reconnection to localized three-dimensional (3D) magnetic field perturbations imposed by a pair of figure-8-shaped coils are investigated in the Magnetic Reconnection Experiment (MRX) device. Both the magnetic field geometry and current sheet profiles are altered by external perturbations. For the case when the inductive electric field associated with these perturbations aligns with the preexisting reconnection electric field, O-type magnetic structures appear within an elongated current sheet. When these magnetic structures are ejected downstream at the speed close to the ion outflow velocity, the inductive electric field is enhanced considerably. Despite that the imposed perturbation amplitude is larger than 30% of the original reconnecting magnetic field, the overall reconnection process remains robust without current sheet disruptions. This technique to form O-type magnetic structures can serve as an additional experimental knob for future systematic laboratory investigations of 3D magnetic reconnection and related instabilities without disrupting two-dimensional current sheet.

Published under an exclusive license by AIP Publishing. <https://doi.org/10.1063/5.0187992>

I. INTRODUCTION

Magnetic reconnection rapidly converts stored magnetic energy into the kinetic, thermal, and non-thermal energy of plasmas.^{1–3} Magnetic reconnection plays a crucial role in numerous space and fusion plasma phenomena involving explosive energy release, such as solar flares,^{4,5} magnetospheric substorms,⁶ and sawtooth oscillations in Tokamaks.⁷

The first quantitative model of magnetic reconnection in two-dimensional (2D) geometry has been proposed by Sweet and Parker.^{8,9} Since then, significant theoretical and experimental^{2,10–13} progresses have been made in the past decades based on the conventional 2D geometry to understand the fast and impulsive reconnection process. However, the realistic reconnection is fundamentally three-dimensional (3D) in nature. Therefore, it is important to address under which conditions and how the 3D dynamics fundamentally alter reconnection processes.^{14–16}

A multitude of plasma waves and turbulence can^{17–21} develop in reconnection, resulting in variations along the third dimension (out-of-the-plane direction).²² The reconnection rate can be affected by the presence of waves or turbulence, e.g., via generating anomalous resistivity.²³ Wave-particle interactions also provide new avenues for the conversion of magnetic energy stored in reconnection.²⁴ Moreover, the 3D system permits different boundary conditions (not only periodic as in 2D systems), such as line-tied boundaries occurring in the solar flare reconnection.²⁵ The line-tied boundary plays an important role in the evolution of reconnection process²⁶ and modifies the kink instability dynamics,^{27–30} possibly relevant to the onset and energy dissipation processes during reconnection.

Studying 3D reconnection via satellite observations and numerical simulations is challenging, either because of limited spatial measurement locations along satellite orbits³¹ or the required enormous, even unrealistic, computation resources to conduct some 3D simulations.^{22,32} In

laboratory reconnection experiments, rich 3D behaviors have been observed.^{33–39} However, these 3D dynamic behaviors were spontaneously excited by either plasma instabilities or spatial non-uniformity, not occurring in a controlled manner, which is one important advantage of laboratory experiments over satellite observations and numerical simulations, i.e., enabling the systematic and parametric studies.^{40,41} In this paper, the original 2D symmetry in the Magnetic Reconnection Experiment (MRX) device is broken with an external electromagnetic field produced by two additional loop coils. It is found that the external inductive electric field is capable of locally modifying the reconnection process, providing a controllable platform to investigate 3D magnetic reconnection in laboratory plasmas.

The arrangement for this paper is as follows. The experimental setup in MRX to introduce localized 3D perturbations using two loop coils is described in Sec. II. The dynamic plasma responses to these perturbations are presented in Sec. III, including the change of reconnection magnetic field geometry and current sheet profiles. Interestingly, O-type magnetic structures are formed and ejected downstream at the speed close to ion outflow velocity. Finally, a brief summary is given in Sec. IV.

II. EXPERIMENTAL APPARATUS

A. Figure-8-shaped coils to generate local 3D perturbations

The experiments reported here were conducted in the Magnetic Reconnection Experiment (MRX) device.⁴² As is shown in Fig. 1(a), hydrogen plasmas and the reconnection magnetic field topology are established by toroidal field (TF) coils and poloidal field (PF) coils, respectively, which are embedded in two toroidally symmetric flux cores (gray). The cylindrical coordinates $r - \phi - z$, with z pointing to the left in Fig. 1(a), are adopted in this experiment. The flux cores are of major radius 37.5 cm and are separated along z by a distance of 40 cm. The current waveforms I_{PF} and I_{TF} of coils PF and TF, generated by pulsed power sources, are plotted as solid and dashed black lines in Fig. 1(b). For the pull-phase reconnection experiments reported here,⁴² the reconnection current and electric field are in the $-\phi$ direction. The 2D generalized Sweet–Parker models are sufficient to describe normal reconnection processes in MRX.⁴³

To break the 2D symmetry of reconnection in MRX, two additional figure-8-shaped insulated coils with a radius of 5 cm are inserted in between two flux cores at a specific toroidal angle, $\phi = \phi_0 = 0^\circ$, see Fig. 1(a). Each coil is centered at $R = 37.5$ cm, $Z = \pm 11$ cm. One main advantage of the figure-8-shaped over single O-shaped coils is that X-type in-plane magnetic field geometry is formed around the current sheet center, resembling to the preexisting reconnection magnetic field geometry formed by two flux cores.

Two different loop current configurations are defined as the aid-pull and anti-pull cases depending on the direction of coil current I_{Loop} . The I_{Loop} configuration of the aid-pull case is plotted in the inset panel of Fig. 1(a), showing that the coils provide an inductive electric field in vacuum $E_{i,loop}$ along $-\phi$, which aligns parallel to preexisting reconnection current and reconnection electric field E_0 , when I_{Loop} ramps up. The anti-pull configuration is implemented by reversing the I_{Loop} direction. The evolution of magnetic field (B_r, B_z, B_ϕ) is measured with spatial resolution of 2 cm along R and 3 cm along Z by magnetic probe arrays placed at the ϕ_0 plane. The figure-8-shaped coils are supported by a movable rack mounted in the chamber, capable of varying

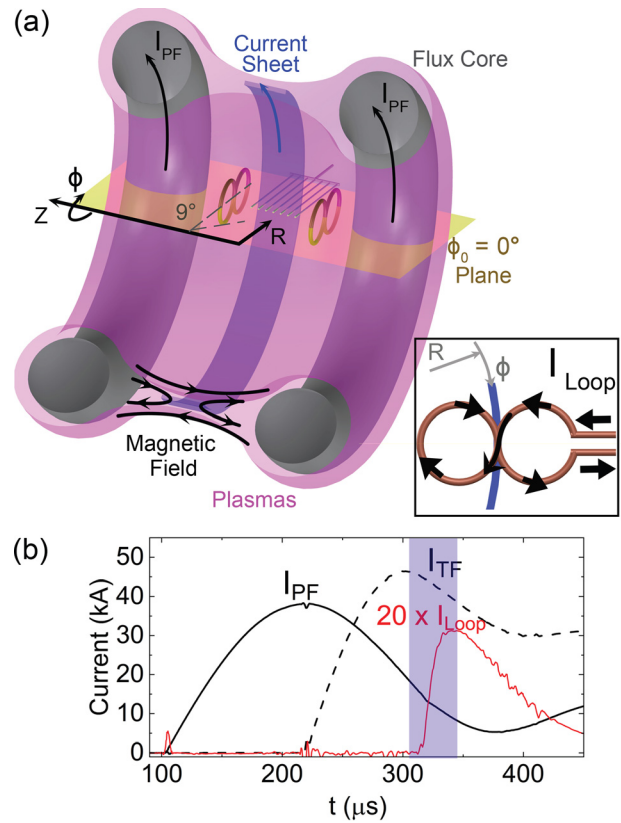


FIG. 1. (a) Two flux cores carrying poloidal (I_{PF}) and toroidal (I_{TF} , not shown) pulsed current form the reconnection magnetic field geometry (black vectors) and plasmas (magenta). The current sheet (blue) is of same direction to I_{PF} during the pull-type reconnection. Two figure-8 shaped coils are inserted at the $\phi_0 = 0^\circ$ plane to create 3D perturbations. In the inset panel, black arrows denote coil current I_{Loop} direction in the aid-pull configuration. One magnetic probe array in the (r, z) plane is used to measure reconnection magnetic field geometry. (b) The typical discharge current waveforms of I_{PF} (black solid line), I_{TF} (black dashed line), and I_{Loop} (red solid line). The shaded range represents the typical pull-reconnection phase.

the relative separation between the loops and the probe array in ϕ direction. I_{Loop} is set to ramp up during the normal pull-phase reconnection, denoted by the blue shading in Fig. 1(b).

B. Vacuum magnetic field and inductive electric field

The vector potential \mathbf{A} of two figure-8-shape coils in vacuum is calculated by superposing vector potential arising from each of four circular closed current loops. The inductive electric field is derived as $-\partial\mathbf{A}/\partial t$. The scalar inductive electric field $E_{i,loop}$ is defined with the magnitude of $-\partial A_\phi/\partial t$ and with the sign of $-\partial A_\phi/\partial t$. Figures 2(a) and 2(b) show the spatial profiles of $E_{i,loop}$ normalized to $-\mu_0 dI_{Loop}/dt$, where μ_0 is the vacuum permeability, at ϕ_0 and $\phi_{-1} = 9^\circ$ (near the loop bottom) planes, respectively. $E_{i,loop}$ peaks at $R = 37.5$ cm since the current of similar direction crosses $R = 37.5$ cm, $Z = \pm 11$ cm twice. The signs of $E_{i,loop}$ around $R = (37.5 \pm 10)$ cm are opposite because the current direction is reversed at $R = (37.5 \pm 10)$ cm, $Z = \pm 11$ cm. Figure 2(c) clearly shows that $E_{i,loop}$ diminishes quickly away from the ϕ_0 plane. So

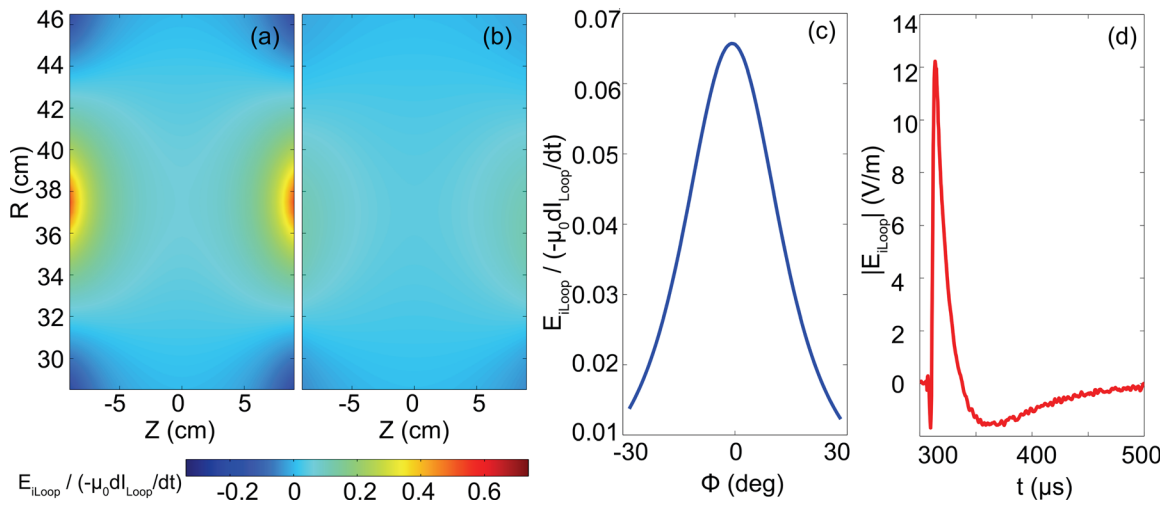


FIG. 2. The calculated inductive electric field profile $E_{i,loop}(R, Z)$ at ϕ_0 (a) and ϕ_{-1} (b) planes in vacuum. (c) $E_{i,loop}$ at $R = 37.5$ cm, $Z = 0$ cm as a function of ϕ . (d) The temporal evolution of $E_{i,loop}$ at $R = 37.5$ cm, $Z = 0$ cm, and $\phi = 0^\circ$ based on the measured loop current waveform.

the perturbation to the original reconnection process caused by these coils is localized around the ϕ_0 plane.

The temporal evolution of $|E_{i,loop}|$ at $R = 37.5$ cm, $Z = 0$ cm, and $\phi = 0^\circ$ is shown in Fig. 2(d), calculated based on the measured dI_{loop} in Fig. 1(b). When the loop current change rate dI_{loop}/dt is at maximum during the current ramp phase at $t \sim 320 \mu\text{s}$, the $E_{i,loop}$ reaches its peak value ~ 12 V/m, which is about 10% of the normal reconnection electric field.

The measured vacuum magnetic profiles on different ϕ planes at $t = 342 \mu\text{s}$, around the peak of I_{Loop} , are given in Fig. 3. Around the center of current sheet, all magnetic field components produced by the figure-8-shaped coils at ϕ_0 and ϕ_{-1} planes approach zero. This geometry is favored due to its negligible modification to the reconnection geometry around the center of current sheet. Only in regions near the edge of coils, there exist significant B_z and B_r components. At the ϕ_0 plane, the in-plane magnetic field is of X-type, and the out-of-plane component B_ϕ is negligible. At the ϕ_{-1} plane, B_r and B_z decrease while B_ϕ increases substantially with a quadrupolar-like profile. This quadrupole B_ϕ profile is of opposite signs at positive and negative ϕ locations due to the opposite radial current directions. The enhancement and suppression of existing quadrupolar Hall magnetic field in reconnection probably cancel out.

III. PLASMA RESPONSES TO LOCAL PERTURBATIONS

A. Modification of reconnection magnetic structure

The in-plane reconnection magnetic field in the presence of plasmas measured on the ϕ_0 plane at $335 \mu\text{s}$ is plotted in Figs. 4(a)–4(d) for the anti-pull case, in Figs. 4(e)–4(h) for the reference case without perturbations, and in Figs. 4(i)–4(l) for the aid-pull case. The magnetic field components B_z , B_r , and B_ϕ and the toroidal plasma current density j_ϕ are color coded in each row of Fig. 4. Considerable modifications to B_r and B_z components are observed near the coil locations $Z = \pm 11$ cm. Intuitively, both B_z and B_r in Figs. 4(a) and 4(b) are enhanced in the anti-pull case because the current direction at $R = 37.5$ cm, $Z = \pm 11$ cm is same with I_{PF} in flux cores. On the

contrary, in the aid-pull case, B_z and B_r are decreased, even reversed in the far downstream regions of reconnection.

The asymptotic B_z values are changed by 30% compared to the reference case, which is comparable to the vacuum magnetic field strength, indicating that the shielding effect of plasmas to the coils are not effective in this experiment. Perturbations caused by the loops are even amplified slightly in the presence of plasmas. One possible explanation is that plasmas behave like a magnetic flux conserver, capable of compressing and further increasing the magnetic field strength.

As is shown in Fig. 4(g), the quadrupole Hall magnetic field B_ϕ profile is produced by Hall-regime magnetic reconnection.^{44,45} The basic pattern of B_ϕ is retained in both anti-pull and aid-pull cases, see Figs. 4(c) and 4(k). It is also interesting to note that even with this large perturbation ($>30\%$), the reconnection current sheet still remains intact, without being interrupted or disrupted. This highlights the robustness of axisymmetric boundaries arising from two toroidally symmetric flux cores in MRX.

B. Formation and ejection of O-type magnetic structures

During the normal pull-reconnection process, a current sheet is formed with J_ϕ along $-\phi$, see Fig. 4(h). The change of current sheet profile at the ϕ_0 plane under perturbations of loop coils is limited to the region near the coil locations $Z = \pm 11$ cm. For the aid-pull case, the reversal of B_z and B_r at downstream of the current sheet forms locally closed magnetic field geometries, corresponding to four localized current channels. These downstream current channels are denoted by four gray ellipses in Fig. 4(l), corresponding to the regions with reversed B_z as in Fig. 4(i). On the other hand, for the anti-pull case, no additional localized current channels exist, as shown in Fig. 4(d). The calculation of j_ϕ around coil edges is not reliable because the spatial resolution of magnetic field measurements 4 cm is too coarse for calculating spatial gradient values in this region with the characterized gradient length of magnetic field <5 mm.

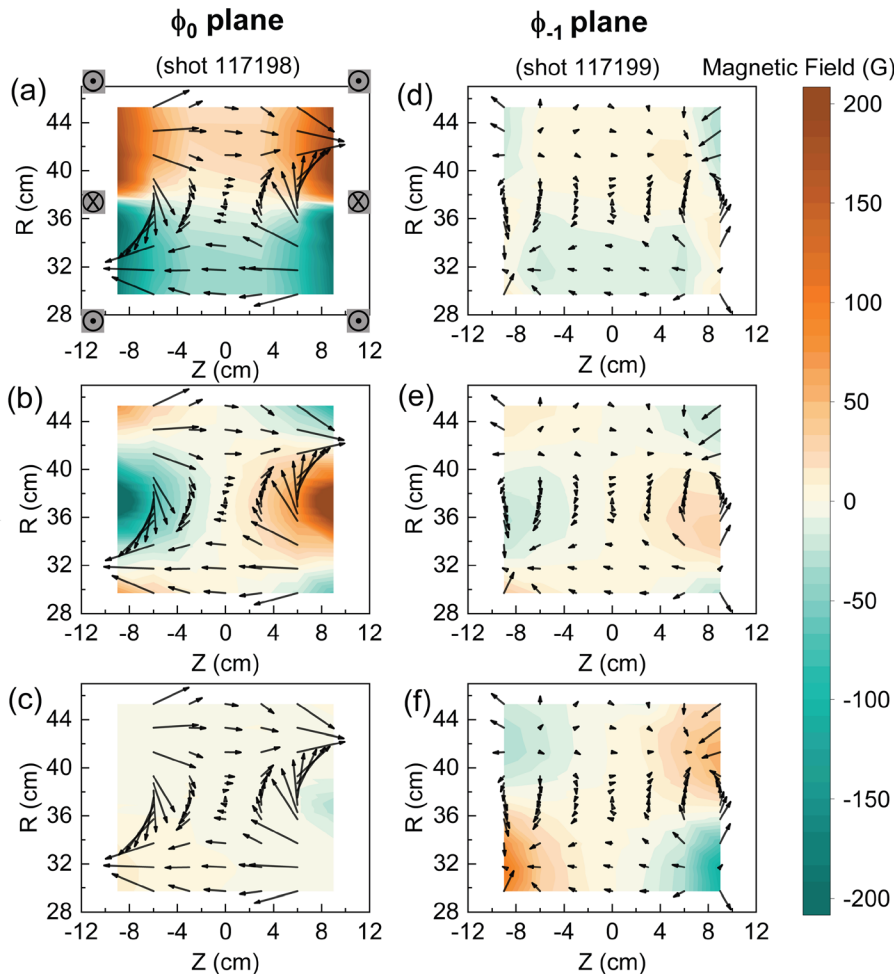


FIG. 3. The in-plane vacuum magnetic field geometry (black arrows) and three different magnetic field components (background colors), i.e., B_z (a), B_r (b), and B_ϕ (c), generated by the loop coils for the anti-pull case measured at the ϕ_0 plane. (d)–(f) Similar to (a)–(c), but measured at the ϕ_{-1} plane. The location and directions of the coil current are also denoted in (a).

Whereas the modification to current density profile at ϕ_0 plane is mostly dominated by the direct coupling or addition of vacuum coil magnetic field, the plasma response can be more readily demonstrated by measurements at ϕ_{-1} plane, where the coil magnetic field is negligible. Figure 5 provides the temporal evolution of current density profile at ϕ_{-1} plane for the aid-pull case. The O-type magnetic field structure denoted by the white line in Fig. 5(a) resembles to one magnetic island, accompanied by locally enhanced current density.³⁶ The presence of O-type magnetic structures temporally correlates with the active perturbations when the coil loop current ramps up from 320 to 340 μs . Notably this O-type magnetic structure travels toward downstream at the speed of ~ 10 km/s, approximately close to the ion outflow velocity.⁴⁶ This implies that O-type magnetic structures are coupled with the reconnection process and are ejected downstream together with the ion outflow.

No O-type magnetic structures are observed in the anti-pull case and reference case, as are presented in Fig. 6. Comparing to the reference case, the current sheet is less elongated in the anti-pull case, while more elongated in the aid-pull case. The elongated current, i.e., a large aspect ratio L/δ , where L and δ are half-width and half-thickness of the current sheet, respectively, renders reconnection more likely prone to tearing instabilities.^{47–49} It is worth noting that these O-type

magnetic structures are not conventional magnetic islands or plasmoids arising from tearing or plasmoid instability in reconnection, mainly because the formation of these structures is likely due to forced responses of preexisting reconnection to externally imposed excessive electric field, rather than the natural tearing instabilities occurring when L/δ is larger than the threshold value ~ 100 for collisional multiple X-line reconnection.^{10,50,51} However, at the same time, it should be pointed out that the threshold L/δ can be lowered in the presence of nonideal effects, e.g., excessive reconnection electric field and electron-scale dynamics.⁵² Therefore, further studies are required to determine if tearing instabilities could play a role in the formation of these O-type magnetic structures.

Note that the reconnection under localized 3D perturbations exhibits 3D or non-axisymmetric features, which can be revealed by different magnetic field and toroidal plasma current profiles at different ϕ planes, see Figs. 4 and 6. The reconnection magnetic field strength at ϕ_0 plane is larger (smaller) than that at ϕ_{-1} plane for the anti-pull (aid-pull) case. For the anti-pull case, the axial extent of current sheet along the outflow direction is smaller at ϕ_0 plane, compared to ϕ_{-1} plane. The ejected O-type magnetic structure is observed only at ϕ_{-1} plane for the aid-pull case.

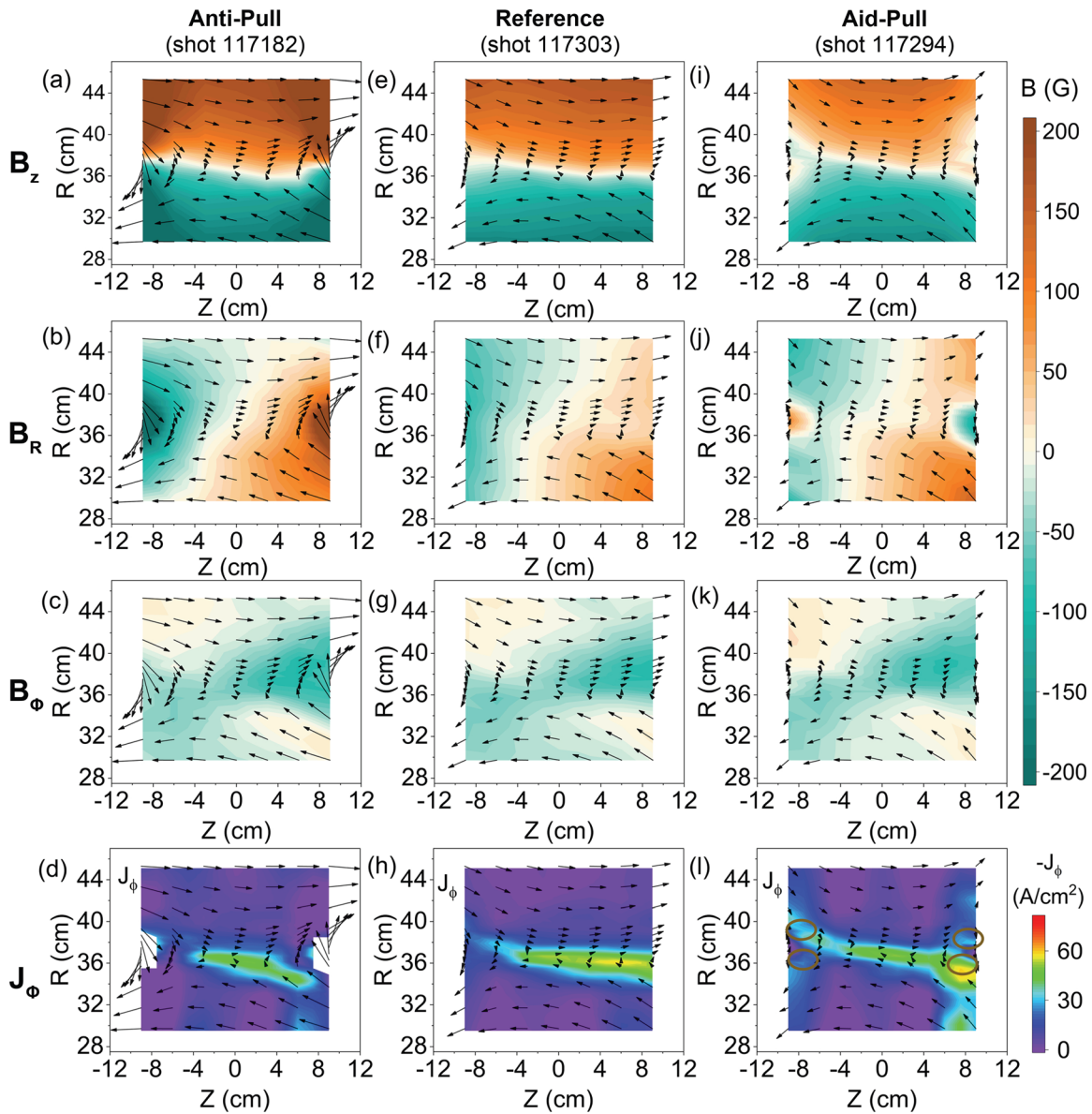


FIG. 4. The in-plane magnetic field geometry (black arrows), three different magnetic field components (background colors) including B_z (a), B_r (b), and B_ϕ (c), and toroidal plasma current density J_ϕ (d) measured at the ϕ_0 plane for the anti-pull case. (e)–(h) Similar to (a)–(d), but measured for the reference case without perturbation fields. (i)–(l) Similar to (a)–(d), but measured for the aid-pull case. Four gray ellipses in panel (l) denote regions with reversed B_z and localized current channels.

C. Change of inductive reconnection electric field

The figure-8-shaped coils are expected to generate toroidal inductive electric field, modifying the original reconnection. The relation between the appearance and ejection of O-type magnetic structures and inductive electric field $E_{i\phi}$ is investigated.

For the normal axisymmetrical reconnection in MRX, the inductive electric field $E_{i\phi} = -\partial A_\phi / \partial t$, where vector potential $A_\phi = \psi / 2\pi r$ and ψ is the magnetic flux function of in-plane magnetic field components. In a 3D reconnection, the line integral of parallel electric field along magnetic field lines passing through the

diffusion region is used to characterize the occurrence of reconnection.^{16,53} The aforementioned derivation of $E_{i\phi}$ via ψ does not apply. However, we note that the 3D perturbation is localized in our experiments because the coil diameter 10 cm \ll the total current sheet length 235 cm along ϕ . The global reconnection can still be roughly treated as in the 2D case. Also note that the deviation of actual $E_{i\phi}$ from the value obtained from aforementioned methods is proportional to the ratio between current sheet thickness ($\sim 1 - 2$ cm) and the spatial scale of magnetic field variation (\sim coil diameter 10 cm).⁵⁴ Therefore, in the spirit of qualitatively characterizing reconnection,

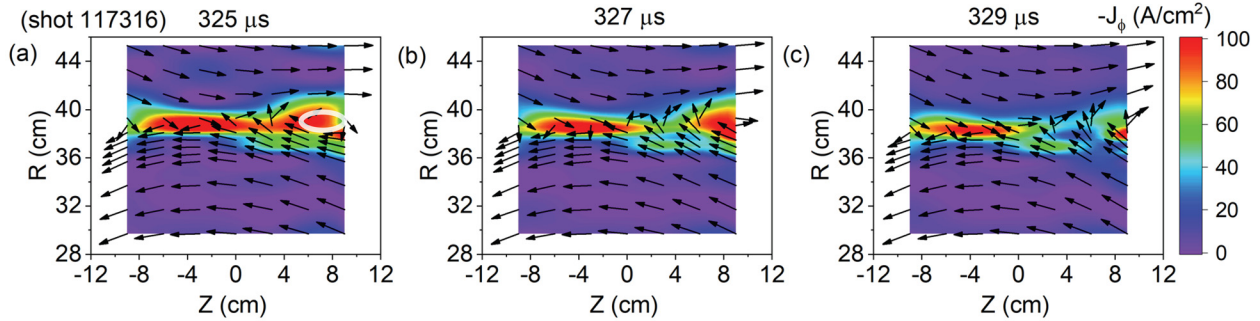


FIG. 5. The temporal evolution of the toroidal current density profile $J_\phi(R, Z)$ and in-plane magnetic field geometry (black arrows whose length is proportional to the logarithm of its magnitude) measured on the ϕ_{-1} plane for the aid-pull case, at $t = 325$ (a), 327 (b), and $329 \mu\text{s}$ (c). Clear signature of moving O-type internal structures is denoted by the white ellipse.

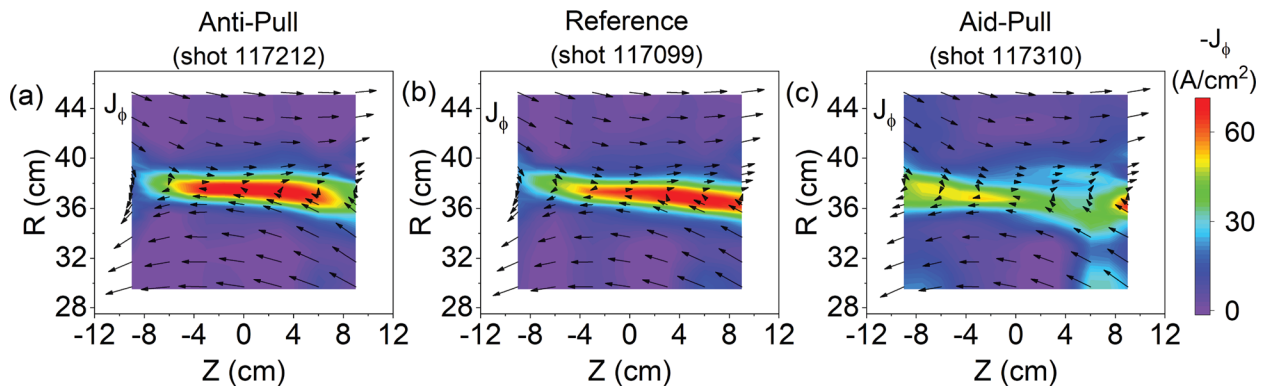


FIG. 6. The toroidal current density J_ϕ and in-plane magnetic field (black vector arrows) measured at the ϕ_{-1} plane at $t = 335 \mu\text{s}$ for the anti-pull (a), reference (b), and aid-pull (c) cases.

we calculate E_{rec} via $-\partial A_\phi / \partial t$ in an approximate manner as used in 2D reconnection.

Figure 7 presents the spatial distribution of $E_{i\phi}$ during the ejection of one O-type magnetic structure in the aid-pull case, as shown in Fig. 5. Maximal $E_{i\phi}$ resides in between the primary current sheet (left) and the ejected O-type magnetic structure. The locations of maximal $E_{i\phi}$ shift toward downstream as this structure is being ejected. The

$\mathbf{E} \times \mathbf{B}$ drift velocity 20–30 km/s is qualitatively comparable to the ejection speed ~ 10 km/s, suggesting that $E_{i\phi}$ is possibly relevant to the ejection of O-type magnetic structures.

Since the induced electric field aligns with preexisting reconnection electric field, larger maximal $E_{i\phi}$ value of 150 V/m is achieved compared to normal reconnection electric field $E_{i\phi} \sim 100 - 120$ V/m. Taking into consideration that the reconnection magnetic field is approximately

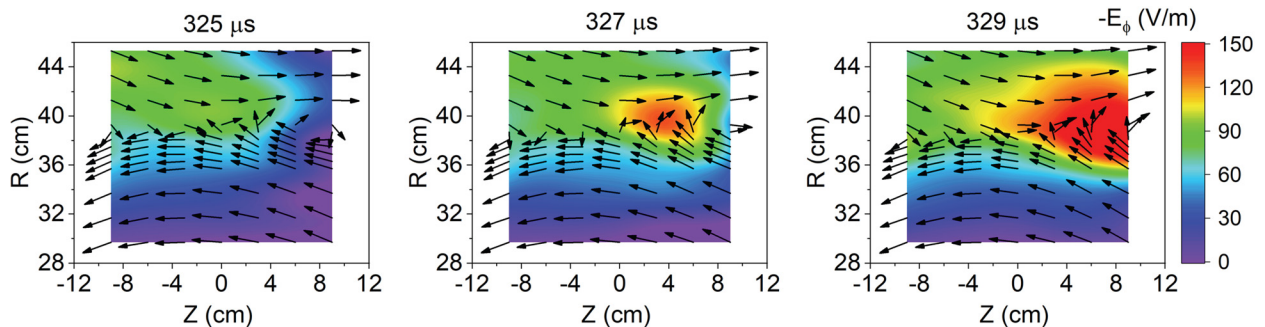


FIG. 7. The time evolution of the toroidal inductive electric field profile $E_{i\phi}(R, Z)$ and in-plane magnetic field geometry (black arrows whose length is proportional to the logarithm of its magnitude) at ϕ_{-1} plane for the aid-pull case, at $t = 325$ (a), 327 (b), and $329 \mu\text{s}$ (c).

same, see Figs. 6(b) and 6(c), the reconnection rate^{55,56} is larger under aid-pull perturbations. In the meanwhile, the Ohmic dissipation power $E_{i\phi}J_\phi$ is increased, consistent with the formation of O-type magnetic structures, which provides additional magnetic energy dissipation sites in between primary current sheet and secondary closed magnetic structures.

D. Temporal evolution as a dynamic process

The externally imposed perturbations occur in relatively shorter time scales compared to preexisting reconnection, which can be seen as external impulses of magnetic and inductive electric field. The plasma responses to these external impulses are expected to be dynamic in nature. As are demonstrated in Figs. 5 and 7, J_ϕ and $E_{i\phi}$ profiles evolve as the O-type magnetic structure is being ejected downstream, i.e., no quasi-static states are achieved during the plasma response.

Moreover, external perturbations must penetrate through plasmas before being coupled to reconnection. The penetration time scales determine whether responses are Alfvénic or diffusive. In the vacuum case, there exists a quadrupole-like B_ϕ profile at the ϕ_{-1} plane, as shown in Fig. 3(f). Figure 8 shows that the temporal evolution of peak values of quadrupole-like B_ϕ profiles (blue line) in vacuum syncs with I_{Loop} (red line), as expected. In the presence of plasmas, the reconnection process itself will produce a quadrupole $B_{\phi hall}$ field due to the Hall effect,^{44,45} see Fig. 4(g). For the anti-pull case, B_ϕ on the ϕ_{-1} plane is enhanced by the coils-generated component. Subtracting $B_{\phi hall}$ from measured B_ϕ in plasma, the plasma response component ΔB_ϕ induced by the loops is obtained and plotted as the green solid line in Fig. 8.

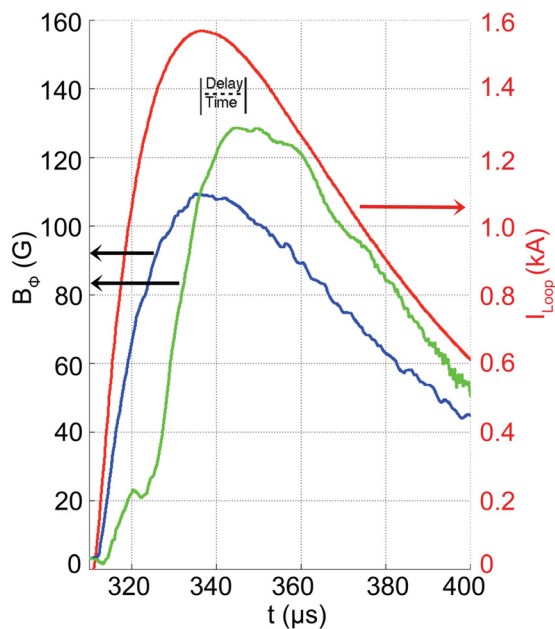


FIG. 8. The plasma response to the loops with a pulsed current: red is the loop current waveform; blue is the peak value of quadrupole-like $B_\phi(R, Z)$ on the ϕ_{-1} plane in vacuum; green is the peak value of B_ϕ on the ϕ_{-1} plane in plasmas after subtracting B_ϕ due to Hall effects.

The time delay between peaks of ΔB_ϕ and I_{Loop} is $\tau \sim 15 \mu s = 6\tau_A$, given that the Alfvén time τ_A is estimated to be $2.5 \mu s$ for a typical scale length of 10 cm, B_z of 120 G, and density of $5 \times 10^{13} \text{ cm}^{-3}$. τ is significantly smaller than the magnetic diffusion time around 0.4 ms, implying that the impulsive perturbation field penetrates into plasmas more likely through a dynamic process instead of a diffusion process.

IV. SUMMARY

Two figure-8-shaped loop coils are placed in downstream regions of magnetic reconnection in MRX to generate localized 3D magnetic and electric field perturbations to modify the normal pull-reconnection process by breaking its 2D symmetry along the toroidal direction. Two loop coil current configurations are investigated, i.e., aid- (anti-) pull case when the inductive toroidal electric field aligns parallel (anti-parallel) to the original reconnection electric field. The plasmas dynamically response to these externally imposed perturbations, occurring at the Alfvén timescale. In the aid-pull case, O-type magnetic structures resembling to magnetic islands appear inside the elongated current sheet. Notably, the O-type magnetic structures are ejected downstream at the velocity close to the ion outflow speed. This phenomenon is likely correlated with the local enhancement of inductive electric field in regions between the primary current sheet and the ejected magnetic structure.

The figure-8-shaped coils provide one additional laboratory knob to systematically investigate local 3D reconnection physics in 2D symmetric reconnection devices, e.g., FLARE (Facility for Laboratory Reconnection Experiments).⁵⁷ However, no disruption of current sheet at global scales is observed yet even when the externally imposed magnetic field perturbation is $>30\%$ of original reconnection field strength. The robustness feature of reconnection might be related to axisymmetrical boundaries controlled by two flux cores in MRX. It remains unexplored how reconnection responses to external perturbations on global scales as a function of perturbation geometry and magnitude, which can also be investigated complementarily via numerical simulations.⁵⁸

ACKNOWLEDGMENTS

This work was supported by the U.S. Department of Energy’s Office of Fusion Energy Sciences under Contract No. DE-AC0209CH11466 and by NASA under Grant Nos. NNH15AB29I and 80HQTR21T0105.

AUTHOR DECLARATIONS

Conflict of Interest

The authors have no conflicts to disclose.

Author Contributions

Jinlin Xie: Conceptualization (equal); Data curation (equal); Formal analysis (equal); Investigation (equal); Validation (equal); Visualization (equal); Writing – original draft (equal); Writing – review & editing (equal). **Peiyun Shi:** Data curation (equal); Formal analysis (equal); Investigation (equal); Validation (equal); Visualization (equal); Writing – original draft (equal); Writing – review & editing (equal). **Hantao Ji:** Conceptualization (equal); Funding acquisition (lead); Project administration (equal); Resources (equal); Supervision (equal); Validation (equal); Writing – review &

editing (equal). **Jonathan Jara-Almonte**: Conceptualization (equal); Investigation (equal); Writing – review & editing (equal). **Jongsoo Yoo**: Conceptualization (equal); Investigation (equal); Validation (equal); Writing – review & editing (equal). **Yukehi Okunishi**: Formal analysis (equal); Writing – review & editing (equal). **Seth Dorfman**: Writing – review & editing (equal). **Masaaki Yamada**: Conceptualization (equal); Supervision (equal); Writing – review & editing (equal).

DATA AVAILABILITY

The data that support the findings of this study are available from the corresponding author upon reasonable request.

REFERENCES

- ¹M. Yamada, R. Kulsrud, and H. Ji, *Rev. Mod. Phys.* **82**, 603 (2010).
- ²M. Hesse and P. A. Cassak, *J. Geophys. Res.: Space Phys.* **125**, e2018JA025935, <https://doi.org/10.1029/2018JA025935> (2020).
- ³H. Ji, W. Daughton, J. Jara-Almonte, A. Le, A. Stanier, and J. Yoo, *Nat. Rev. Phys.* **4**, 263 (2022).
- ⁴S. Krucker, H. S. Hudson, L. Glesener, S. M. White, S. Masuda, J.-P. Wuelser, and R. P. Lin, *Astrophys. J.* **714**, 1108 (2010).
- ⁵G. D. Fleishman, G. M. Nita, B. Chen, S. Yu, and D. E. Gary, *Nature* **606**, 674 (2022).
- ⁶V. Angelopoulos, J. P. McFadden, D. Larson, C. W. Carlson, S. B. Mende, H. Frey, T. Phan, D. G. Sibeck, K.-H. Glassmeier, U. Auster *et al.*, *Science* **321**, 931 (2008).
- ⁷M. Yamada, F. M. Levinton, N. Pomphrey, R. Budny, J. Manickam, and Y. Nagayama, *Phys. Plasmas* **1**, 3269 (1994).
- ⁸P. A. Sweet, *Electromagnetic Phenomena in Cosmical Physics* (1958), Vol. **6**, p. 123.
- ⁹E. N. Parker, *J. Geophys. Res.* **62**, 509, <https://doi.org/10.1029/JZ062i004p00509> (1957).
- ¹⁰Z. W. Ma and A. Bhattacharjee, *Geophys. Res. Lett.* **23**, 1673, <https://doi.org/10.1029/96GL01600> (1996).
- ¹¹M. Hesse, K. Schindler, J. Birn, and M. Kuznetsova, *Phys. Plasmas* **6**, 1781 (1999).
- ¹²J. Birn, J. F. Drake, M. A. Shay, B. N. Rogers, R. E. Denton, M. Hesse, M. Kuznetsova, Z. W. Ma, A. Bhattacharjee, A. Otto, and P. L. Pritchett, *J. Geophys. Res.: Space Phys.* **106**, 3715, <https://doi.org/10.1029/1999JA900449> (2001).
- ¹³H. Ji, J. Yoo, W. Fox, M. Yamada, M. Argall, J. Egedal, Y.-H. Liu, R. Wilder, S. Eriksson, W. Daughton *et al.*, *Space Sci. Rev.* **219**, 76 (2023).
- ¹⁴D. I. Pontin, *Adv. Space Res.* **47**, 1508 (2011).
- ¹⁵T. Li, E. Priest, and R. Guo, *Proc. R. Soc. A* **477**, 20200949 (2021).
- ¹⁶D. I. Pontin and E. R. Priest, *Living Rev. Sol. Phys.* **19**, 1 (2022).
- ¹⁷Y. V. Khotyaintsev, D. B. Graham, C. Norgren, and A. Vaivads, “Collisionless Magnetic Reconnection and Waves: Progress Review,” *Front. Astron. Space Sci.* **6**, 70 (2019).
- ¹⁸B. N. Rogers, R. E. Denton, J. F. Drake, and M. A. Shay, *Phys. Rev. Lett.* **87**, 195004 (2001).
- ¹⁹T. A. Carter, H. Ji, F. Trintchouk, M. Yamada, and R. M. Kulsrud, *Phys. Rev. Lett.* **88**, 015001 (2001).
- ²⁰P. Shi, K. Huang, Q. Lu, and X. Sun, *Plasma Phys. Controlled Fusion* **61**, 125010 (2019).
- ²¹J. Yoo, J.-Y. Ji, M. V. Ambat, S. Wang, H. Ji, J. Lo, B. Li, Y. Ren, J. Jara-Almonte, L.-J. Chen *et al.*, *Geophys. Res. Lett.* **47**, e2020GL087192, <https://doi.org/10.1029/2020GL087192> (2020).
- ²²W. Daughton, V. Roytershteyn, H. Karimabadi, L. Yin, B. J. Albright, B. Bergen, and K. J. Bowers, *Nat. Phys.* **7**, 539 (2011).
- ²³H. Ji, S. Terry, M. Yamada, R. Kulsrud, A. Kuritsyn, and Y. Ren, *Phys. Rev. Lett.* **92**, 115001 (2004).
- ²⁴Y. Ren, L. Dai, C. Wang, and B. Lavraud, *Astrophys. J.* **928**, 5 (2022).
- ²⁵P. C. Grigs and A. O. Benz, *Astrophys. J.* **625**, L143 (2005).
- ²⁶J. A. Robertson and E. R. Priest, *Sol. Phys.* **114**, 311 (1987).
- ²⁷I. Furno, T. P. Intrator, D. D. Ryutov, S. Abbate, T. Madziwa-Nussinov, A. Light, L. Dorf, and G. Lapenta, *Phys. Rev. Lett.* **97**, 015002 (2006).
- ²⁸A. L. Moser and P. M. Bellan, *Nature* **482**, 379 (2012).
- ²⁹C. E. Myers, M. Yamada, H. Ji, J. Yoo, W. Fox, J. Jara-Almonte, A. Savcheva, and E. E. DeLuca, *Nature* **528**, 526 (2015).
- ³⁰P. Shi, P. Srivastav, C. Beatty, R. John, M. Lazo, J. McKee, J. McLaughlin, M. Moran, M. Paul, E. E. Scime *et al.*, *Phys. Plasmas* **28**, 032101 (2021).
- ³¹R. B. Torbert, I. Dors, M. R. Argall, K. J. Genestreti, J. L. Burch, C. J. Farrugia, T. G. Forbes, B. L. Giles, and R. J. Strangeway, *Geophys. Res. Lett.* **47**, e2019GL085542, <https://doi.org/10.1029/2019GL085542> (2020).
- ³²Y.-H. Liu, T. C. Li, M. Hesse, W. J. Sun, J. Liu, J. Burch, J. A. Slavin, and K. Huang, *J. Geophys. Res.: Space Phys.* **124**, 2819, <https://doi.org/10.1029/2019JA026539> (2019).
- ³³E. E. Lawrence and W. Gekelman, *Phys. Rev. Lett.* **103**, 105002 (2009).
- ³⁴T. P. Intrator, X. Sun, G. Lapenta, L. Dorf, and I. Furno, *Nat. Phys.* **5**, 521 (2009).
- ³⁵N. Katz, J. Egedal, W. Fox, A. Le, J. Bonde, and A. Vrublevskis, *Phys. Rev. Lett.* **104**, 255004 (2010).
- ³⁶S. Dorfman, H. Ji, M. Yamada, J. Yoo, E. Lawrence, C. Myers, and T. D. Tharp, *Geophys. Res. Lett.* **40**, 233, <https://doi.org/10.1029/2012GL054574> (2013).
- ³⁷F. Fan, Q. Zhang, L. Sang, W. Ding, and J. Xie, *Chin. Phys. Lett.* **36**, 015201 (2019).
- ³⁸S. Greess, J. Egedal, A. Stanier, W. Daughton, J. Olson, A. Lê, R. Myers, A. Millet-Ayala, M. Clark, J. Wallace *et al.*, *J. Geophys. Res.: Space Phys.* **126**, e2021JA029316, <https://doi.org/10.1029/2021JA029316> (2021).
- ³⁹P. Shi, P. Srivastav, M. H. Barbhuiya, P. A. Cassak, E. E. Scime, and M. Swisdak, *Phys. Rev. Lett.* **128**, 025002 (2022).
- ⁴⁰G. G. Howes, *Phys. Plasmas* **25**, 055501 (2018).
- ⁴¹Y. Liu, P. Shi, X. Zhang, J. Lei, and W. Ding, *Rev. Sci. Instrum.* **92**, 71101 (2021).
- ⁴²M. Yamada, H. Ji, S. Hsu, T. Carter, R. Kulsrud, N. Bretz, F. Jobses, Y. Ono, and F. Perkins, *Phys. Plasmas* **4**, 1936 (1997).
- ⁴³H. Ji, M. Yamada, S. Hsu, and R. Kulsrud, *Phys. Rev. Lett.* **80**, 3256 (1998).
- ⁴⁴Y. Ren, M. Yamada, S. Gerhardt, H. Ji, R. Kulsrud, and A. Kuritsyn, *Phys. Rev. Lett.* **95**, 055003 (2005).
- ⁴⁵M. Yamada, Y. Ren, H. Ji, J. Breslau, S. Gerhardt, R. Kulsrud, and A. Kuritsyn, *Phys. Plasmas* **13**, 52119 (2006).
- ⁴⁶J. Yoo, M. Yamada, H. Ji, and C. E. Myers, *Phys. Rev. Lett.* **110**, 215007 (2013).
- ⁴⁷H. P. Furth, J. Killeen, and M. N. Rosenbluth, *Phys. Fluids* **6**, 459 (1963).
- ⁴⁸L. C. Lee and Z. F. Fu, *J. Geophys. Res.: Space Phys.* **91**, 6807, <https://doi.org/10.1029/JA091iA06p06807> (1986).
- ⁴⁹D. Biskamp, *Phys. Fluids* **29**, 1520 (1986).
- ⁵⁰K. Shibata and S. Tanuma, *Earth, Planets Space* **53**, 473 (2001).
- ⁵¹N. F. Loureiro, A. A. Schekochihin, and S. C. Cowley, *Phys. Plasmas* **14**, 100703 (2007).
- ⁵²J. Jara-Almonte, H. Ji, M. Yamada, J. Yoo, and W. Fox, *Phys. Rev. Lett.* **117**, 95001 (2016).
- ⁵³W. Gekelman, T. De Haas, W. Daughton, B. Van Compernelle, T. Intrator, and S. Vincena, *Phys. Rev. Lett.* **116**, 235101 (2016).
- ⁵⁴S. E. Dorfman, “Experimental study of 3-D, impulsive reconnection events in a laboratory plasma,” Ph.D. thesis (Princeton University, 2012).
- ⁵⁵P. A. Cassak, Y.-H. Liu, and M. A. Shay, *J. Plasma Phys.* **83**, 715830501 (2017).
- ⁵⁶Y.-H. Liu, P. Cassak, X. Li, M. Hesse, S.-C. Lin, and K. Genestreti, *Commun. Phys.* **5**, 97 (2022).
- ⁵⁷H. Ji, R. Cutler, G. Gettelfinger, K. Gilton, A. Goodman, F. Hoffmann, J. Jara-Almonte, T. Kozub, J. Kukon, G. Rossi *et al.*, in APS Division of Plasma Physics, 2018.
- ⁵⁸A. Stanier, W. Daughton, A. Le, X. Li, and R. Bird, *Phys. Plasmas* **26**, 072121 (2019).